Advances and challenges for fluorescence nanothermometry

Jiajia Zhou[1], Blanca del Rosal[2], Daniel Jaque[3], Seiichi Uchiyama[4], Dayong Jin[1]

[1] Institute for Biomedical Materials & Devices (IBMD), Faculty of Science, University of Technology Sydney, Sydney, Australia

[2] ARC Centre of Excellence for Nanoscale Biophotonics, RMIT University, Melbourne, Australia

[3] Nanobiology Group, Instituto Ramón y Cajal de Investigación Sanitaria, IRYCIS, Madrid, Spain

[4] Graduate School of Pharmaceutical Sciences, The University of Tokyo, Tokyo, Japan

E-mail: daniel.jaque@uam.es

Advances and Challenges for Fluorescence Nanothermometry

Jiajia Zhou[1,*], Blanca del Rosal[2], Daniel Jaque[3,4,*], Seiichi Uchiyama[5], Dayong Jin[1,6]

[1] *Institute for Biomedical Materials & Devices (IBMD), Faculty of Science, University of Technology Sydney, Sydney, Australia*
[2] *ARC Centre of Excellence for Nanoscale Biophotonics, RMIT University, Melbourne, Australia*
[3] *Nanobiology Group, Instituto Ramón y Cajal de Investigación Sanitaria, IRYCIS, Madrid, Spain*
[4] *Fluorescence Imaging Group, Departamento de Física de Materiales – Facultad de Ciencias, Universidad Autónoma de Madrid, Madrid, Spain*
[5] *Graduate School of Pharmaceutical Sciences, The University of Tokyo, Tokyo, Japan*
[6] *Department of Biomedical Engineering, Southern University of Science and Technology, Guangdong, P.R. China*
*E-mail: jiajia.zhou@uts.edu.au; daniel.jaque@uam.es

Fluorescent nanothermometers can probe the change of local temperature in living cells and *in vivo*. This field attracts major international efforts in developing both temperature-responsive materials and detection procedures to achieve sub-degree temperature resolutions in biosystems. The newly demonstrated nanothermometers have shown superior sensing performance and multifunctionality, which enables state-of-the-art functional imaging techniques towards improved spatial, temporal, and temperature resolutions for monitoring metabolism of intracellular organelles and internal organs. While the technology becomes mature, along with some debatable records, recent studies have also shown that these nanoscopic thermometers could come across possible biased sensing during the fluorescence-based detection. In this review, we introduce the design principle and advances of fluorescence nanothermometry, discuss the scenarios that may lead to biased sensing, analyze the challenges ahead from both fundamental levels and their practical implementations, and propose new directions to improve the mutual understandings of this interdisciplinary research field.

1. Introduction

Materials that possess fluorescence properties strongly dependent on temperature could be used for far-field, contactless and high-sensitivity readout of thermal field changes at the nanoscale{Jaque, 2012 #118}, which are the foundation of current nanothermometry. Such materials are referred to as (fluorescent) nanothermometers. The possibility of contactless nanothermometry with a sub-micrometric resolution has found numerous applications in different fields such as nanofluidics[1], catalytic reactions[2], microelectronics[3, 4], and most importantly cell biology and pre-clinical research and diagnostics[5-11]. Nanothermometers have enabled unthinkable challenges such as the measurement of intracellular temperature or the early detection of tumors through remote thermal monitoring{Zhou, 2016 #119}{Suzuki, 2020 #120}. These potentials have attracted numerous researchers to work on the design and synthesis of temperature-sensitive nanomaterials[9-13]. Advanced physicochemical synthesis routes have led to new temperature-dependent properties being discovered from a range of different materials. A collection of nanothermometers have been made with both high thermal sensitivity, and pre-selected spectral operation ranges. The proof-of-concept demonstrations have shown promises of using nanothermometers in cell biology research and *in vivo* diagnostics.

Because the performance of nanothermometers employing different sensing strategies has been evaluated based on diversified assessment protocols and in different conditions, the potential use of fluorescence nanothermometry as a robust tool for either cell biology research or animal studies has not been fully demonstrated. Moreover, biased sensing appears along with the complex *in vivo* environment. In this review, we survey mechanisms based on photophysical properties and temperature sensing strategies of fluorescent materials, evaluate the recent progress of nanothermometers for intracellular temperature detection and *in vivo* diagnostics, and point out the aspects that cause biased readouts. We discuss the challenges and opportunities in developing new-generation nanothermometer materials and state-of-the-art imaging techniques towards improved spatial, temporal, and temperature resolutions for monitoring metabolism of intracellular organelles and internal organs.

2. Design Principles and Advances of Fluorescent Nanothermometers

In the past ten years, materials with temperature-responsive fluorescence and biocompatible surface have been developed as nanothermometers for noncontact intracellular and *in vivo* temperature monitoring. These materials include organic species such as fluorescent proteins (FPs), small organic compounds (dyes), lanthanide complexes, dye-doped polymeric nanoparticles, and inorganic nanoparticles including quantum dots (QDs), lanthanide ions doped nanoparticles (Ln-NPs), nitrogen-vacancy (NV) containing nanodiamonds (NDs), carbon dots (CDs), and others. Their temperature sensing features, for which the commonly involved indicators are defined in Box 1, will be discussed in sections 2.1, 2.2 and 2.3.

2.1 Sensing strategies and design of nanothermometers

Nanothermometers show their characteristic response to the temperature by elaborating on their

---

Box 1 | Glossary of terms used and performance comparison of fluorescent nanothermometers

In all fluorescence-based strategies, temperature is calculated from the measurement of diverse indicators, such as intensity, intensity ratio, peak position, polarization and lifetime. The value of these fluorescence indicators can be quantified as Q.

The rate of the change of Q associated with temperature T is defined as **sensing sensitivity**: $S = \left| \frac{\partial Q}{\partial T} \right|$ (1).

To compare the fluorescent nanothermometers with different indicators, the **relative sensitivity** is used: $S_R = \left| \frac{1}{Q} \frac{\partial Q}{\partial T} \right|$ (2). S_R is comparable between different systems with the consistent unit of K^{-1}, $°C^{-1}$, or %/K, %/°C.

The **uncertainty** comes from random variations in replicated independent measurements (type A) and systematic effects in the measurement process (type B).
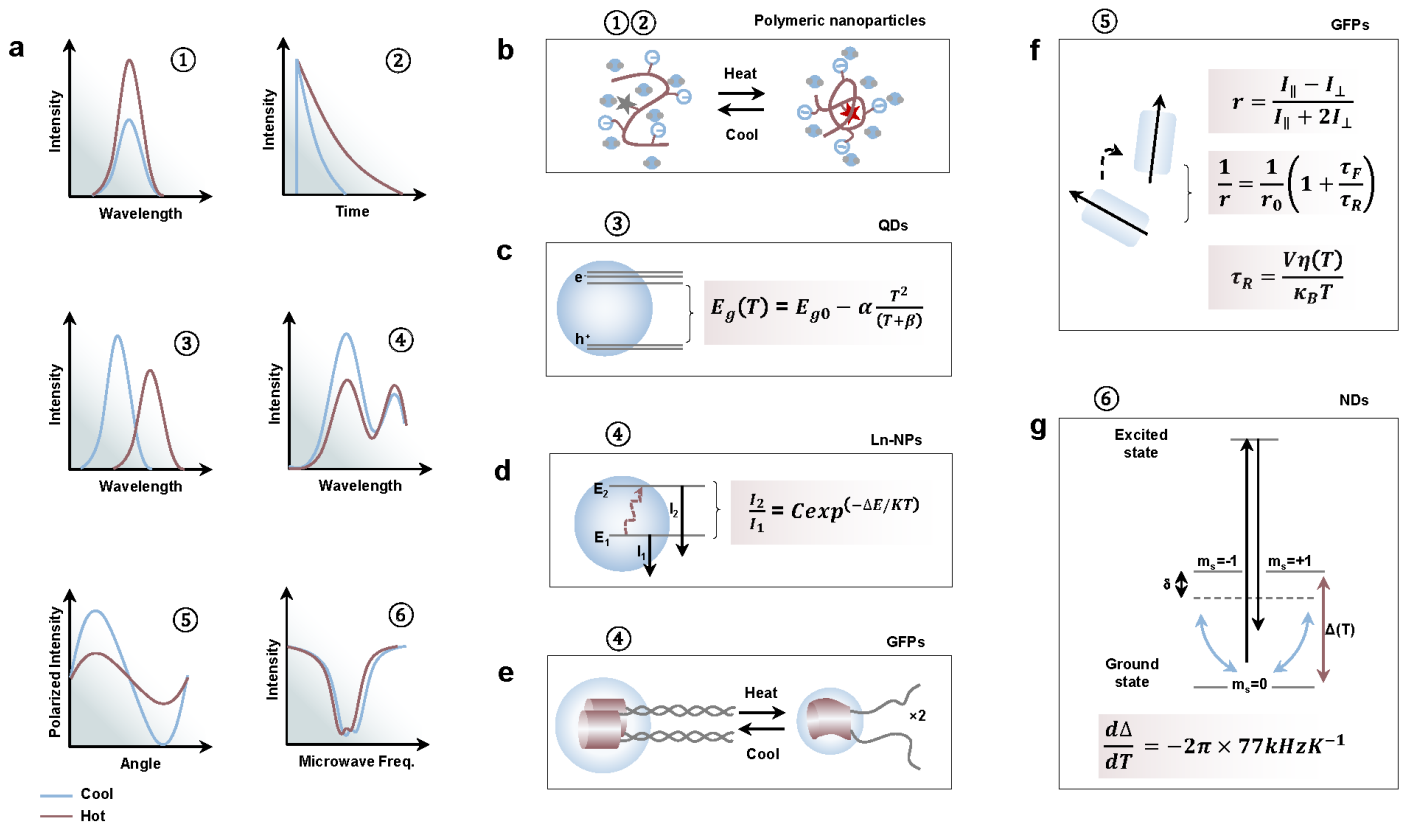
Temperature resolution is the smallest change in a temperature that causes a perceptible change in the fluorescence indicator: It is expressed by $\Delta T_{min} = \frac{\sigma}{S}$ (3), in which σ is the standard deviation of the parameter used for temperature determination.

Spatial resolution is the minimum distance between points of a measurement that can be resolved under the temperature resolution of the system, and can be calculated as $\Delta x_{min} = \frac{\Delta T_{min}}{\left| \frac{dT}{dx} \right|}$ (4).

Temporal resolution is the minimum period of time between measurements capable of resolving a temperature higher than the temperature resolution, and calculated as $\Delta t_{min} = \frac{\Delta T_{min}}{\left| \frac{dT}{dt} \right|}$ (5).

Note that except for the S_R, all other parameters included in the box not only depend on the fluorescent nanothermometer themselves, but also on the experimental setup used and the biological system under evaluation.

molecular, atomic, and even electronic scale dynamics. These dynamics are phenomenologically measurable through different optical indicators such as emission intensity, peak position, emission/excitation intensity ratio, lifetime, polarization anisotropy, and electron spin resonance (ESR)/optically detected magnetic resonance (ODMR) (Figure 1a).

$$r = \frac{I_\parallel - I_\perp}{I_\parallel + 2I_\perp}$$

$$\frac{1}{r} = \frac{1}{r_0}\left(1 + \frac{\tau_F}{\tau_R}\right)$$

$$\tau_R = \frac{V\eta(T)}{\kappa_B T}$$

$$E_g(T) = E_{g0} - \alpha\frac{T^2}{(T+\beta)}$$

$$\frac{I_2}{I_1} = C exp^{(-\Delta E/KT)}$$

$$\frac{d\Delta}{dT} = -2\pi \times 77 kHz K^{-1}$$

Figure 1 | Typical temperature sensing strategies and mechanisms in different nanothermometers. a, Temperature sensing strategies relying on the emission intensity (①), lifetime (②), peak position (③), emission/excitation intensity ratio (④), fluorescence polarization anisotropy (⑤) and electron spin resonance (ESR)/optically detected magnetic resonance (ODMR) (⑥). **b,** The NNPAM unit in polymeric nanoparticles shrinks to release water molecules at an elevated temperature, which leads to the emission intensity enhancement and lifetime extension. **c,** Bandgap change of quantum dots at an elevated temperature, leading to the peak shift, bandwidth broadening, and lifetime shortening. The temperature-dependent bandgap can be described by Varshni's empirical expression, in which Eg_0 is the energy gap at 0 K, α is the temperature coefficient, and value β is close to the Debye temperature of the material. **d,** The electrons in the lower-lying excited state (E_1) are thermally populated to the higher excited state (E_2) in Ln-NPs, leading to the emission intensity ratio increase at elevated temperatures. The emission intensity ratio obeys the Boltzmann distribution, in which C is a constant, ΔE is the energy gap between the two excited states, k is the Boltzmann constant, and T is the absolute temperature. **e,** Conformational change of GFP-tagged proteins at an elevated temperature, leading to the excitation intensity ratio change of GFP fluorescence. **f,** Molecular rotation (such as GFP) arising from Brownian dynamics given by Perrin's equation, which means that an increase of temperature contributes to lower fluorescence polarization anisotropy (r). The fluorescence polarization anisotropy can be monitored by polarized fluorescence. $I_\parallel$ and $I_\perp$ are the intensities of the polarized fluorescence parallel and perpendicular to the incident polarization, r_0 the fundamental or limiting anisotropy, τ_F the fluorescence lifetime, τ_R the rotational correlation time, $\eta(T)$ the dynamic viscosity of the medium, V the hydrodynamic molecular volume and k_B the Boltzmann constant. **g,** At zero magnetic field, the ground-state spin |m_s=±1> sublevels of nitrogen-vacancy in nanodiamonds are split from the |m_s=0> state by a temperature-dependent zero-field splitting $\Delta(T)$ due to thermally induced lattice strains. The spin states can be coherently manipulated using microwave pulses and efficiently initialized and detected using laser illumination.

The intensity-temperature relationship allows temperature sensing (①in Figure 1a) if the fluorescence intensity depends solely on the surrounding temperature. The most obvious approach — thermal quenching — exists in small organic molecules, in which temperature increasing induces quenching of fluorescence intensity[14]. On the contrary, special design to use a water-sensitive fluorescent polymer unit and heat trigger for water molecule release facilities the enhanced fluorescence from 20 °C to 50 °C (Figure 1b)[8]. These polymeric nanoparticles have been used to evidence the temperature difference between the nucleus and cytoplasm in living COS7 cells. However, the different concentrations of the nanothermometers in nucleus and cytoplasm influence the local fluorescence intensity, which indicates that the temperature difference identified from the intensity could be wrong. An alternative method is to use the lifetime of polymeric nanoparticles (②in Figure 1a), which prolonged from 4 ns to ~ 9 ns when the temperature increased from 20 °C to 40 °C, irrespective of the concentration of nanothermometers.

Fluorescence lifetime imaging microscopy has been widely used for diverse nanothermometers that show relevant temperature-dependent lifetime feature. For example, silicon nanoparticles[15] showed decreasing lifetime from 23 ns down to 8 ns as the temperature increased from 0.5 °C to 60 °C, due to the thermally favored nonradiative processes involving both vibrations and rotations of surface ligands. Temperature activation of nonradiative relaxation was also observed in CDs[16], in which the lifetime decreased from 11 ns to 5.3 ns as the temperature increased from 2 °C to 80 °C.

Temperature-induced spectral shift (③in Figure 1a) widely exists in semiconducting QDs, in which the bandgap of QDs changes with temperature following Varshni's expression $E_g(T) = E_{g0} - \alpha T^2/(T+\beta)$ (Figure 1c)[17]. Thermally induced narrowing of the bandgap correlates to the redshift of the spectral peak, which is always accompanied by an intensity reduction. Different from the intensity, the spectral shift versus temperature is independent of the QD local concentration and thus the two-photon fluorescence thermal imaging of CdSe has been reported to measure the intracellular temperature with a sensitivity of 0.16 nm/°C[18]. Particle size-dependent spectral shift has been further observed in CdTe QDs, with a sensitivity range of $0.2 - 0.8$ nm/°C[19].

Ratiometric thermometry involves the change in the ratio of either emission or excitation intensities from two peaks (④in Figure 1a). The prevalence of ratiometric design is due to its relatively high resistance to environmental interference. In Ln-NPs, the thermally coupled energy levels, E_1 and E_2, as shown in Figure 1d, allow remote thermal sensing. By measuring the emission intensity ratio (I_2/I_1), the absolute temperature can be deduced according to the Boltzmann distribution equation $I_2/I_1 = C exp^{(-\Delta E/KT)}$ (Figure 1d). The full knowledge of the physical mechanisms behind the thermal sensitivity allows checking for the presence of possible artifacts and makes possible absolute temperature readouts, leading to what is known as primary thermometers. Typical thermal coupling energy level pairs include Er^{3+} ($^2H_{11/2}$ and $^4S_{3/2}$)[20], Nd^{3+} ($^4F_{5/2}$ and $^4F_{3/2}$)[21], and Eu^{3+} ($^5D_1$ and $^5D_0$)[22]. Excitation intensity ratio based sensing has been demonstrated using green fluorescent proteins (GFPs), in which the change of the excitation ratio could be tuned by conformational changes of GFP-tagged proteins (Figure 1e)[6].

Fluorescence polarization anisotropy (FPA) (⑤in Figure 1a) is defined as a ratio ($r = (I_\parallel - I_\perp)/(I_\parallel + 2I_\perp)$) related to the emission intensity collection from both the parallel and perpendicular polarizations with respect to the incident polarization. The measured FPA is closely related to molecular rotation arising from Brownian dynamics according to Perrin's equation $1/r = 1/r_0 (1 + \tau_F/\tau_R)$ (Figure 1f). Small molecular nanothermometers such as GFPs and organic dyes have such dynamic FPA[23, 24], in which the increasing temperature contributed to the smaller FPA due to a faster rotation of the molecules (Figure 1f).

This relation was expressed by Debye-Stokes-Einstein equation $\tau_R = V_\eta(T)/K_B T$.

The ESR and ODMR based sensing strategies refer in particular to vacancy containing diamond nanothermometers (⑥ in Figure 1a)[5, 25]. As shown in Figure 1g, each NV center has a ground state spin-triplet (m_s=0, ±1). At the zero magnetic field, the transition frequency (Δ) between the $|m_s=0\rangle$ and $|m_s=\pm1\rangle$ states (m_s, spin projection) has a temperature dependence of $d\Delta/dT = -2\pi \times 77 kHzK^{-1}$ [5]. This means that a temperature rise shifts the Δ to a lower frequency, in which the exact frequency could be optically measured with the coherent control using microwave pulses. By recording the spectral shift of the zero-phonon lines of NV centers, NDs could also be used for temperature sensing[26].

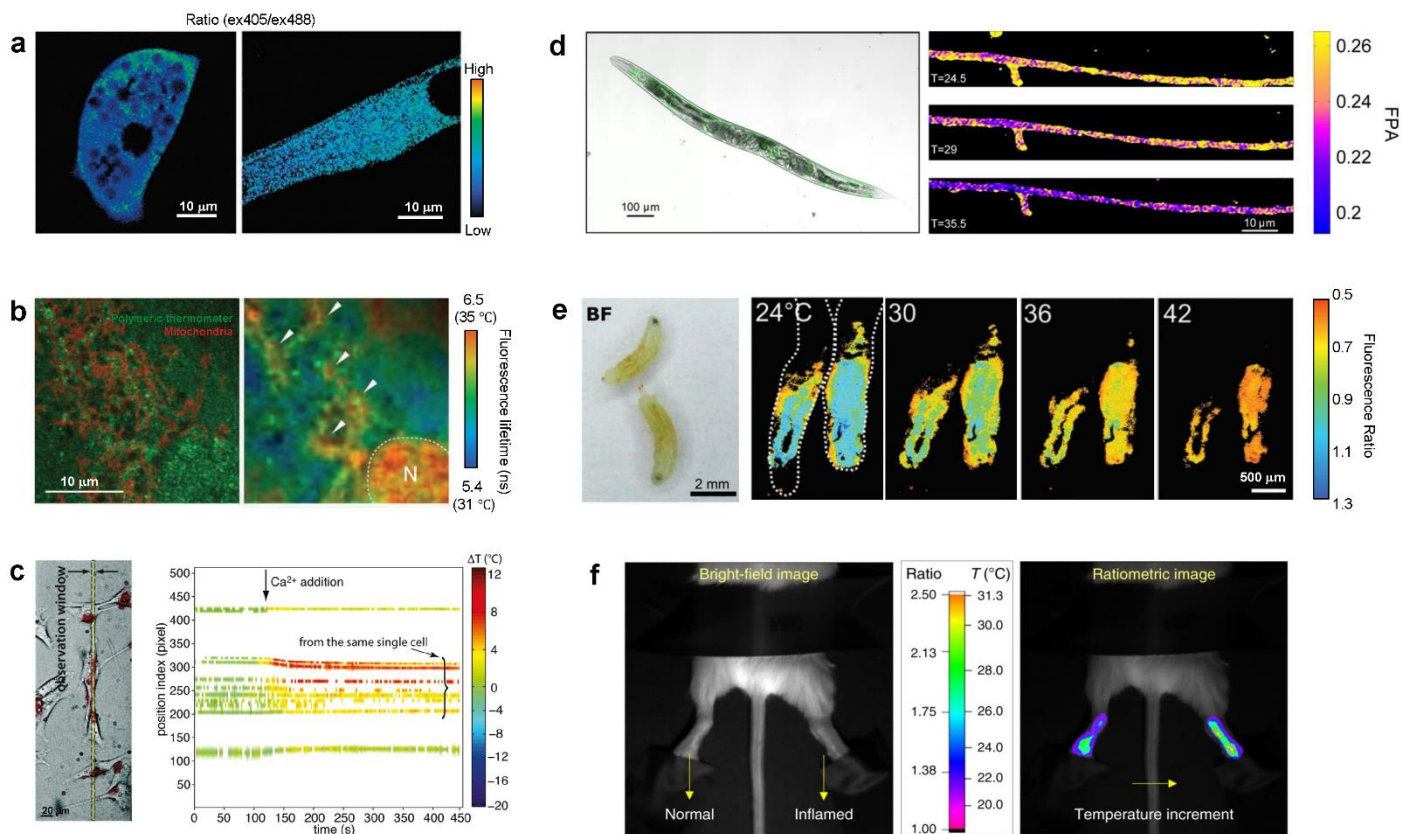## 2.2 Progress in intracellular temperature sensing

When nanothermometers are delivered into biological cells by endocytosis, chemical diffusion, or microinjection, intracellular temperature can be measured. If nanothermometers have a structure which targets organelles, it is possible to detect local temperature changes related to organelle functions. Most nanothermometers, particularly the ones based on nanoparticles, undergo a modification in their physical properties to allow cell biology applications due to their limitations in size, biocompatibility and hydrophilicity of their surfaces. The function of nanothermometers in intracellular spaces is frequently validated with a temperature variation in external media, local heating by a laser, and drug stimulation. Novel knowledge, such as organelle-dependent thermogenesis and chemical-induced thermogenesis, has been acquired on cellular biophysics. Some nanothermometers have been used as an established analytical tool in biological research based on traditional techniques (see Box 2).

Box 2 | Fluorescent nanothermometers contributed to biological studies

Some readily available fluorescent nanothermometers with high sensitivity to temperature variations have been used in biological studies as an established tool. A small organic molecular nanothermometer, MitoThermo Yellow measured a mean mitochondria temperature rise in HEK293 cells to be approximately 10 °C under full activation of respiration[14]. DyLight549 molecular thermometer monitored the membrane temperature change during remote control of ion channels and neurons[27]. Brown adipocytes are known to regulate energy expenditure though non-shivering thermogenesis in human, and therefore are emergent targets for treating obesity. Different groups focused on different molecules to activate brown adipocytes for thermogenesis. Fluorescent polymeric nanothermometers accurately monitored the effects of apoptosis signal-regulating kinase 1 (ASK1)[7], a β3-adrenergic receptor agonist CL316.243[28], a natriuretic peptide carperitide[29], and the ER-resident sensor PKR-like ER kinase (PERK)[30] on the thermogenesis of brown adipocytes. In addition, fluorescent polymeric nanothermometers could be applied to intracellular thermometry at the tissue level[31], in which brain ischemia was associated to serious edema through remarkable temperature increases in brain tissue. Though not peer-reviewed, other cases can be found in brown adipocytes with a fluorescent polymeric nanothermometer[32] and in embryos of *C. elegans* with NDs[33].

Fluorescent protein nanothermometers are the most familiar to biologists and advantageous in their superior targeting ability to organelles. The expression-based FPs nanothermometers showed their potential for temperature monitoring in Golgi of HEK 293 cells[27], mitochondria of brown adipocytes (BAs) and endoplasmic reticulum (ER) of myotubes (Figure 2a)[6], mitochondria of HeLa cells[6, 34, 35], as well as whole cancer cell temperature mapping[23, 34]. Nevertheless, the reported thermal sensitivities of FPs remain relatively low (<2.82 %/°C).

Organic fluorescent dyes show both good temperature sensitivity and intracellular targeting ability. Successful localized temperature monitoring using dye nanothermometers include membrane and mitochondria of HEK 293 cells[14, 27], ER and mitochondria of BAs[36, 37], and HCT116 cell spheroids[38]. However, the photostability of dyes varies depending on their structure. For example, the ER thermo yellow nanothermometers suffered from imaging time-induced intensity bleaching with a rate of 1.5%/min[39], in which bleaching correction was required to sense the temperature accurately. ERthermAC has improved photostability[36].

Figure 2 | Typical examples of intracellular and *in vivo* temperature sensing by using fluorescent nanothermometers. a, Subcellular-targeted tsGFP1-mito (left) and tsGFP1-ER (right) with ratiometric pseudocolor images visualize endogenous thermogenesis in brown adipocytes (left) and myotubes (right). **b,** Fluorescent polymeric thermometers reveal local heat production near the mitochondria in living COS7 cells. Confocal fluorescence image (left) of fluorescent polymeric thermometer (green) and MitoTracker Deep Red FM (red) and fluorescence lifetime image of thermometer (right). Arrowheads point to local heat production. N indicates the nucleus. **c,** QDs thermometers reveal heterogeneous local thermogenesis in NIH/3T3 murine fibroblast cells. Left, a bright-field optical transmission micrograph of cells overlaid with QDs emission image, shown in red. Right, location-dependent intracellular temperature progression as a function of time of the same cell shown in the observation window (left). The time point at which ionomycin calcium complex was added, ~120 s, is marked by an arrow. The uncertainties of position localization as estimated from the Gaussian fitting are represented as shades of the temperature color; the more intense and the narrower the vertical distribution, the more accurately the location is. **d,** Fluorescence polarization anisotropy (FPA) of green fluorescent protein allowed in vivo intracellular temperature imaging in *C. elegans.* Left, bright-field image of the C. elegans overlapped with the GFP fluorescence intensity coming from the GABAergic neurons in green. Right, FPA of the same neurons at three temperatures. **e,** The lanthanide complex thermometer and reference dye embedded in a polymeric matrix allowed "temperature mapping" inside a fruit fly larva. Left, a bright field image of two larvae. Right, micro-thermography of larvae using the fluorescence ratio (EuDT/Ir(ppy)$_3$). **f,** Ratiometric thermometry based on a hybrid nanothermometer (TTA-Nd-NPs) measured the inflammation induced temperature increment. Left, bright-filed image showed arthritis in the swollen right leg of a Kunming mouse stimulated with carrageenan (1 wt%, 100 μL) while the left leg was normal as control. Right, ratiometric image revealed the luminescent ratios and evaluated temperature distributions in the two legs.

Panel **a** adapted from ref.[6], ©2013 Nature America, Inc. Panel **b** adapted from ref.[8], ©2012 Macmillan Publishers Limited. Panel **c** adapted from ref.[40], ©2011 American Chemical Society. Panel **d** adapted from ref.[41], ©2013 American Chemical Society. Panel **e** adapted from ref.[42], ©2015 The Royal Society of Chemistry. Panel **f** adapted from ref.[9], © The Author(s) 2018.

A fluorescent nanogel with size around 50 nm was demonstrated for intracellular thermometry in 2009[43]. Through microinjection, the nanothermometers were distributed in the cytoplasm as scattered dots to monitor intracellular temperature with a temperature resolution of 0.29-0.5 °C. However, the large size and low hydrophilicity hindered the homogeneous dispersion of nanothermometers throughout the cell, and thereby the nanogel thermometers failed at mapping the intracellular temperature distribution. In 2012, Okabe and coworkers developed an upgraded linear polymeric nanoparticle with reduced size of 8.9 nm and sufficiently hydrophilic residues[8]. They observed intracellular temperature differences between nucleus, centrosome and cytoplasm through mapping, as well as the local heat production from mitochondria (Figure 2b). To avoid using microinjection to introduce the nanothermometers into cells, cationic polymeric nanoparticles have been recently produced to solve the cell staining problem through cell incubation, which was applicable to yeast cells[44]. Further design of a ratiometric cationic polymer allowed the widespread use of nanothermometers in biological studies (Box 2)[28, 29].

Lanthanide complex based nanothermometers can be made by embedding lanthanide complexes in PMMA with cationic polymer at the surface to form nanoparticles with an average hydrodynamic diameter of circa 200 nm. Reported as "walking nanothermometers"[45], these nanothermometers enclosed in endosomes/lysosomes in living cells after endocytosis can be transported along microtubules. By tracking the position of single nanothermometers, a high spatial localization accuracy of 5.3 nm was achieved. Using the ratiometric design, other lanthanide complex nanothermometers have been demonstrated to perform spot by spot temperature measurements with the application of ionomycin, revealing heterogeneous heat production in a single cell[46].

It is encouraging that a range of inorganic nanothermometers, including QDs, Ln-NPs, NDs, CDs and nanohybrids have been reported for intracellular thermometry with diverse advantages, though various challenges lie ahead. Endocytosed QDs as individual particles sensed the temperature during Ca^{2+} shock with a spatial localization accuracy beyond the optical diffraction limit[40], though the QDs only randomly appear in cytoplasm (Figure 2c). At single-particle level, photobleaching of up to 80% of QDs was observed for QD655 within five minutes[47]. Yb^{3+}, Er^{3+} codoped upconversion nanoparticles (UCNPs) with extremely photostability and detection contrast from negligible background have been reported to monitor the temperature of individual HeLa cells[20]. The challenge for using UCNPs includes the specific labelling of organelles[48] and the parasitic thermal loading. NDs allow the temperature-gradient mapping at the subcellular level, and the challenge includes the requirements of invasive intracellular delivery, *i.e.,* silicon nanowire or needle delivery[5], or long term incubation up to 12h[49].

Despite the rapid progress in developing intracellular nanothermometry, there is a debate about both the detectable temperature heterogeneities and chemical stimulation-induced temperature rises in single living cells[50]. Due to the limit of methods to evaluate the authenticity of the temperature variation, it is necessary to provide an overview of the reported results from different research groups using different nanothermometers and sensing strategies. Table 1 summarizes the progress of intracellular temperature detection, and the variations in detectable temperature were found ranging from sub-1 K to ~10 K, depending on the experimental setups and the biological systems. The average temperature heterogeneity within the cells was found to be smaller than 1 K. Employing other probes or analyses to double-check the physiological response through other indicators can help to confirm the detection of temperature change, for example, to check the mitochondrial depolarization, oxygen consumption, extracellular acidification rate, or use the simulation and inhibition method to recover the temperature change.

Table 1 | Fluorescent nanothermometers for intracellular temperature measurements

Nanothermometers		Sensing strategy*	Entry into cell	Cell lines	Localization	S_R^{max} (T)	ΔT_{min}	Performed stimulation	Feedback	Ref
FPs	tsGFP1-	④	Transfection	HeLa, BAs	Mitochondria	2.82 %/°C	-	CCCP	Heterogeneous thermogenesis correlates	6

	Name	*	Method	Cell	Location	Sensitivity	Resolution	Stimulus	Description	Ref
	mito, tsGFP1-ER, tsGFP1-F						(47 °C)		with electrochemical gradient	
				C2C12	ER			CPA	Visualize SERCA1-mediated thermogenesis in myotubes	
	gTEMP	④	Transfection	HeLa	Mitochondria	1.15 %/°C (34 °C)	0.4 °C	FCCP	Temperature rise of 6-9 °C at the mitochondria matrix	34
					Whole cell		0.1 °C	-	Temperature difference of 2.9±0.3 °C between the cytosol and the nucleus	
	EmGFP-Mito	③	Transfection	HeLa	Mitochondria	2.2 %/°C (23 °C)	0.26 °C (23-39 °C)	FCCP	Mean temperature rise of 3 °C	35
Dyes	ER thermos yellow	①	Incubation at 37 °C for 30 min	HeLa	ER	-	0.2 °C	Ionomycin	Mean temperature rise of 1.6±0.8 °C (6 cells)	39
	ERthermAC	①	Incubation at 37 °C for 30 min	hBAs	ER	-	-	Forskolin	Heterogeneous response (89.7% of responding cells and 10.3% non-responding cells)	36
	RhB-ME and Rh800	④	Incubation at 33 °C for 1h	BAs	Mitochondria	-	-	CCCP	Maximum transient rate of mitochondrial temperature increase is on the order of ~ $10^{-2} - 10^{-1}$ K/s	37
								NE	Heterogeneous response (59.4±15.9% responding cells for 118 cells)	
	Mito-TEM	①	Incubation at 37 °C for 30 min	MCF-7	Mitochondria	-	-	PMA	Temperature rise of 3 °C from 29 to 32 °C within 10 min; slower change rate in the next 20 min	51
	Mito thermo yellow	①	Incubation at 37 °C for 15 min	3T3, HeLa, C2C12, mESC, Chang, BA	Mitochondria	2.0-2.8 %/°C	-	Laser heating	Temperature gradient	52
Polymeric nanoparticles		① ②	Microinjection	COS7	Whole cell	-	0.18-0.58 °C (29-39 °C)	Glucose metabolism	Mean temperature difference of 0.96 °C between nucleus and cytoplasm (62 cells); Cell cycle dependent temperature gap; Centrosome (by 0.75 °C on average) is warmer than cytoplasm	8
								FCCP	Mean temperature change of 1.02±0.17 °C inside COS7 cells for 3o min (7 cells)	
		②	Incubation at 25 °C for 10 min	COS7	Whole cell	-	0.05-0.54 °C (28-38 °C)	CCCP	Mean temperature rise of 1.57±1.41 °C (17 cells)	53
		④	Targeting/incubation for 3h	HeLa	Cytoplasm	-	0.3-0.5 °C (32-39 °C)	Ionomycin	Temperature rise from 34.5 °C to 39 °C within 2 min	54
		④	Targeting/incubation for 3h	HeLa	Mitochondria	-	<0.98±0.08 °C (31-39 °C)	FCCP, Ionomycin	Temperature rise from 32.6 °C to 35 °C within 2 min (75% decrease in ATP), then decrease as the cells shrank (ATP remained unchanged)	55
Lanthanide complex		④	Incubation at 37 °C for 2h	HeLa	Endosomes or lysosomes	-	-	Ionomycin	Mean temperature rise of 1.9±0.8 °C (8 cells); Heterogeneous heat production in degrees, space, and time	46
QDs	QD655	③	Incubation at 37 °C for 1h	NIH/3T3	Cytoplasm	-	-	Ionomycin	Heterogeneous temperature response (31 cells: 23% decrease, 23% no change, 54% rise); Mean temperature change of -0.14±0.15 °C before shock and +1.84±0.27 °C after shock	40
	QD655	④	Incubation at 37 °C for 1h	SH-SY5Y	Cytoplasm	6.3 %/°C	0.098	CCCP	Mean temperature change of 0.94 °C; Mean temperature difference of 1.6 °C between the cell body and a neurite	47

* Each number indicates the type of temperature sensing strategy categorized in Figure 1a.

2.3 Progress in *in vivo* temperature sensing in animal models

Applications of nanothermometers in *in vivo* temperature monitoring are still in their infancy. Proof-of-concept demonstrations of nanothermometers in animal models include temperature-controlled photothermal

therapy and diagnosis of tumors, inflammatory events and pathologies of the cardiovascular system. As summarized in Table 2, inorganic nanoparticles showing near-infrared excitation/emission features provide the opportunity for the high penetration depth imaging through biological tissues. Infrared light can penetrate hundreds of microns through bone tissue, enabling transcranial thermometry.

Table 2 | *In vivo* fluorescence nanothermometry in small animal models

Animal model	Application	Temperature range		Nanothermometers	λ_{exc} (nm)	λ_{em} (nm)	Sensing strategy*	S_R^{max} (T)	Ref
Breast cancer (MDA-MDB-231) xenograft model	PTT with temperature feedback	32 – 53 °C		LaF$_3$:Nd	808	880	④	0.25 %/°C (33 °C)	56
Ovarian carcinoma (HeLa) xenograft	PTT with temperature feedback	20 – 70 °C		NaLuF$_4$:Yb,Er	980	525/545	④	1 %/°C (35 °C)	10
Mouse model of pancreatic carcinoma	Combination PTT and chemotherapy	37 – 46 °C		NaLuF$_4$:Yb,Er	980	525/545	④	1%/°C (35 °C)	11
Healthy mouse model	Study of thermal dynamics	32 – 39 °C	Ln-NPs	LaF$_3$:Nd@LaF$_3$:Yb	790	890/1060	④	0.44%/°C (10 °C)	57
Healthy mouse model	Study of thermal dynamics	32 – 42 °C		LaF$_3$:Yb,Er@LaF$_3$:Yb,Tm	690	1000/1230	④	5%/°C (20 °C)	58
Mouse model of arthritis	Measuring T difference between inflamed and healthy limbs	20 – 31.3 °C		TTA-UCNPs + NaYF$_4$:Nd	635 + 808	550/1060	④	7.1%/°C (22 °C)	9
Squamous cell carcinoma (A431) xenograft	PTT therapy with temperature feedback	30 – 67 °C		PbS/CdS/ZnS	808	1220	①	1%/°C (20 °C)	59
Mouse model of hindlimb ischemia	Ischemia and inflammation monitoring	ΔT ≤ 10 °C	QDs	PbS/CdS/ZnS	808	1220	①	1%/°C (20 °C)	60
Mouse model of melanoma	Tumour diagnosis	ΔT ≤ 7 °C		Ag$_2$S	808	1200	①	3%/°C (28 °C)	61
Mouse model of drug-induced coma	Brain thermometry	-3 °C ≤ ΔT ≤ 4 °C		Ag$_2$S	808	1200	①	3%/°C (28 °C)	62

* Each number indicates the type of temperature sensing strategy categorized in Figure 1a.

For semi-transparent organs, their temperature reading is straightforward, as the same visible-emitting nanothermometers used for cellular thermometry are adequate in this context. Genetically-encoded thermosensitive FPs have enabled studying the response of *C. elegans* (Figure 2d) and bacteria to heating stimuli[41, 63]. A lanthanide complex thermometer and reference dye embedded in a polymeric matrix allowed two-dimensional ratiometric mapping of the body temperature of fly larvae (Figure 2e)[42] and a beetle *Dicronorhina derbyana*[64]. Intensity-based temperature sensing approaches are limited for dynamic systems where the local concentration of nanosensors can fluctuate with time, which is erroneously attributed to temperature variations.

Fluorescence nanothermometry in small animal models has been primarily explored for real-time *in situ* temperature sensing during photothermal therapy (PTT). It is based on either multifunctional nanothermometers or hybrid nanostructures. Multifunctional nanothermometers from a single material display a temperature-sensitive emission but often accompanied by laser-induced heating under excitation at a certain wavelength. Though needing a single light source for therapy, this strategy comes at the expense of low photothermal conversion efficiencies, which requires relatively high doses of thermometer materials and laser

intensities to achieve successful PTT. Materials include Nd^{3+}-doped LaF_3 nanocrystals[56] (the first luminescent nanothermometers used for PTT with intratumoral temperature feedback) and PbS-based QDs. Nd^{3+}-doped nanocrystals show a ratiometric NIR-I temperature-sensitive emission due to the thermal coupling between Stark sublevels. Their photothermal conversion efficiency can be tuned by adjusting the concentration of Nd^{3+} ions. Higher Nd^{3+} concentrations increase the absorption of the excitation light and the probability of de-excitation *via* non-radiative pathways. This results in a higher photothermal conversion at the expense of fluorescence intensity, which leads to a low signal-to-noise ratio in the temperature readout. PbS-based QDs emitting in NIR-II show a better thermal sensitivity (see Table 2), although this intensity-based system intrinsically only allow measuring temperature variations, as other variables, including the QD concentration, also affect the fluorescence intensity. The higher absorbance of QDs leads to lower laser power density requirements for successful thermal therapy (1.5-2 $W·cm^{-2}$, compared with 4 $W·cm^{-2}$ required for Nd: LaF_3 nanoparticles). These power densities remain well above the desirable power densities used with the photothermal agents, such as gold nanorods or graphene-based nanomaterials[65].

Hybrid nanothermometers are composed of two subunits for photothermal heating and temperature sensing independently. Despite needing a rather complex experimental setup, sometimes requiring two laser sources, this strategy allows the decoupling between heating and thermal sensing, so that high photothermal conversion efficiencies can be achieved using non-fluorescent materials. Li's group has demonstrated a series of works focusing on composite nanothermometers-nanoheaters with visible-emitting UCNPs as thermometers. One example is the nanocomposite formed by a temperature-sensitive core ($NaLuF_4$:Yb, Er UCNPs) and a photothermal carbon shell that allowed photothermal therapy at low laser power density of 0.3 $W·cm^{-2}$. Two different wavelengths activated the laser-induced heating (730 nm) and the emission of UCNPs (980 nm). The temperature readout was extracted from the ratio between two thermally coupled emission bands (centred at 525 and 545 nm) of Er^{3+} ions. Another design of a nanocomposite was based on embedding UCNPs in a porous silica matrix together with a dye-based photothermal agent (excited at 730 nm) for combined temperature-controlled chemotherapy and PTT with *in situ* temperature control[11].

Besides monitoring the progress of hyperthermia-based therapies, *in vivo* nanothermometry has been explored as a way to diagnose a disease and monitor its progress. An increase in the local temperature is directly associated with inflammatory responses. A mouse model of inflammation has been used to evaluate the *in vivo* performance of hybrid nanothermometers that combined temperature-sensitive UCNPs with temperature-insensitive Nd-doped nanoparticles in a bovine serum albumin matrix[9]. This hybrid nanothermometers were capable of providing a subcutaneous thermal image of inflamed tissues (Figure 2f).

The major limitation of these particular hybrid systems is their use of visible-emitting UCNPs as temperature reporters, as the great attenuation of visible light by tissues results in very low signal-to-noise ratios. The possibility of undesired laser-induced heating of healthy tissues cannot be ruled out due to the overlap of the 980 nm radiation required for optical excitation of UCNPs with an absorption band of water.

Other diagnostic applications include studying thermal dynamics by monitoring the thermal relaxation of tissues after external heating stimuli. Different NIR-emitting nanothermometers have been used to characterize this process *in vivo* in healthy specimens[57, 58] and in mouse models of ischemia/inflammation[60] and melanoma[61]. Ximendes and coworkers used core/shell LaF_3:Er,Yb@LaF_3:Yb,Tm nanocrystals with a 5%/ºC sensitivity at 20 ºC (the highest sensitivity reported for NIR-emitting nanothermometers) for real-time recording of subcutaneous temperature[58]. The deep penetration of NIR-II light into tissues also allows contactless transcranial temperature sensing. NIR-II-emitting Ag_2S QDs has been recently demonstrated to explore brain temperature and activity in a murine model of coma[62].

3. Discussion on Biased Sensing

For a nanothermometer, there are often certain temperature-independent factors that influence the fluorescence signal, which is the key to be understood to avoid any artifact or biased readout.
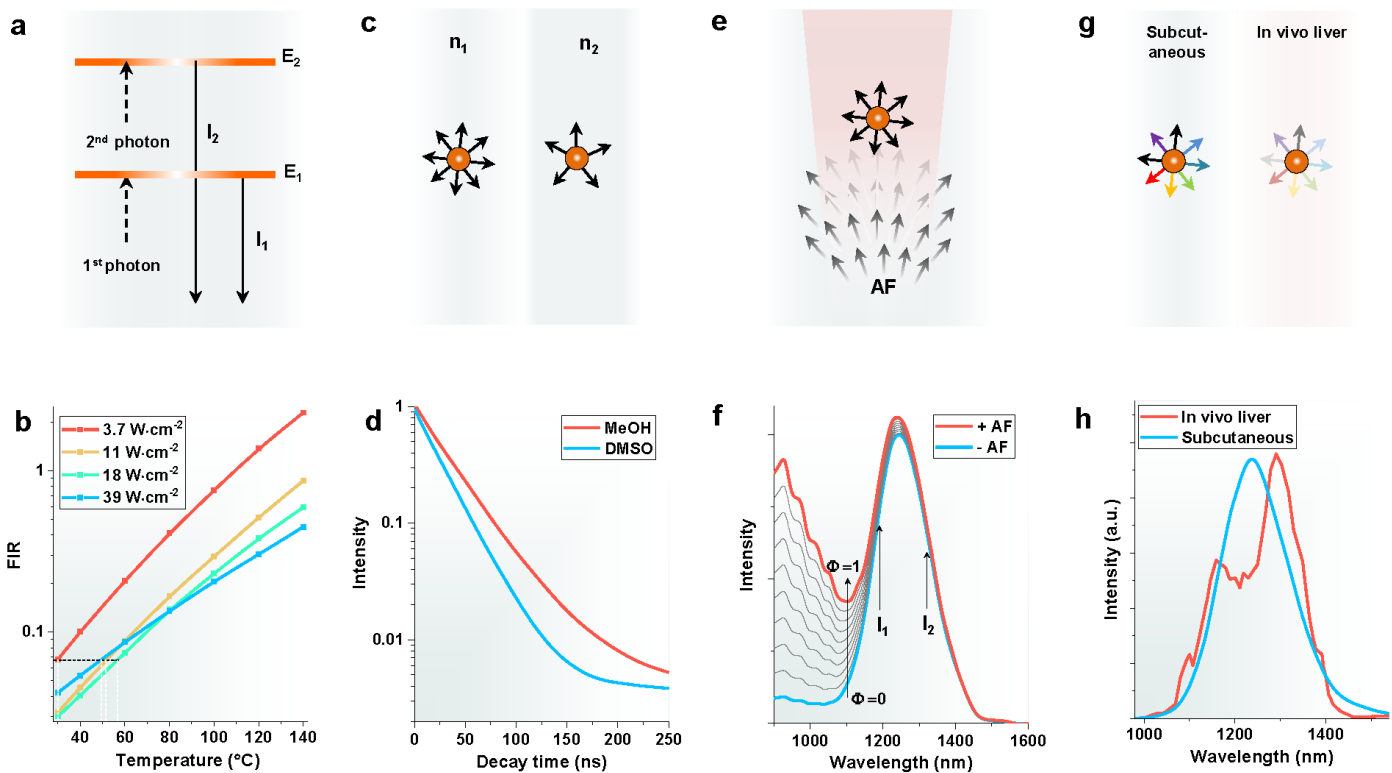
Figure 3 | Factors that often induce artifacts and biased temperature readouts. a and **b,** The FIR from two excited states associated with absorbing different orders of photon numbers (**a**) is highly power-dependent, and thus leads to power-dependent calibration curves for the Nd^{3+}/Er^{3+} based upconversion nanothermometers in ref [3](**b**). **c** and **d,** Colloidal fluorescent nanoparticles exhibit different radiative rate (decay time) (**d**) when the surrounding medium has different refractive indices (**c**). **e** and **f,** The relative weight (Φ) of tissue autofluorescence (AF) affects the readout of fluorescence intensity ratio between two bands (I_1 and I_2). **g** and **h,** Emission spectral variations of Ag_2S QDs in subcutaneous tissue and *in vivo* liver.

Panel **d** adapted from ref. [66], © 2015 American Chemical Society. Panel **h** adapted from ref. [67], © 2020 American Chemical Society.

Bias can be induced by the power-dependent property of fluorescence signals. For example, the ratiometric temperature sensing often involves the intensity detection from two emission materials or the two emission bands of a fluorescence probe, I_1 and I_2. As shown in Figure 3a, if I_1 and I_2 emitted from the excited states E_1 and E_2 follow one-photon linear population process and two-photon upconversion process, respectively, $I_1 \propto$ excitation power density P and $I_2 \propto P^2$ and the fluorescence intensity ratio (FIR) between I_2 and I_1 thereby becomes power dependent, i.e. $I_2/I_1 \propto$ P. If the excitation power density is used differently in the calibration and the actual testing experiment, biased temperature readout will be generated by translating the FIR incorrectly. As shown in Figure 3b, using a lanthanide-based nanothermometer, a one order of magnitude difference in power density will lead to a 30 °C temperature bias. Besides, fluorescent materials, such as organic dyes and QDs, often have large absorption cross section and low quantum yield, which degrades a large faction of absorbed energy to heat though the nonradiative transition upon excitation{Akers, 2011 #121}. Such self-heating induced temperature rise should be evaluated during the calibration experiment.

Bias can be generated due to the change in refractive index values from one organelle to another (Figure 3c). For instance, mitochondria have typical values between 1.4 and 1.42 and the nucleus has values at 1.355 – 1.365[68]. Nanothermometers located in such a heterogeneous environment may behave differently in their electron transition probability and thus emit different optical signals, rather than depend solely on the temperature. As shown in Figure 3d, the lifetimes for a type of Ln-NPs (refractive index 1.8) dispersed in DMSO and methanol are 26 ns and 35 ns, respectively, which is due to the difference in the refractive index of DMSO and methanol, 1.51 and 1.36, respectively[66]. In such a case, bias will be generated when the

temperature for mitochondria is obtained using the lifetime sensing methods based on the same calibration curve established for the nucleus.

The complexity of biological tissues and their interactions with light causes several possible confounding variables, which adds new levels of challenges for temperature sensing in living organs. Bias can be produced by the fluorescence distortion due to the tissue autofluorescence (Figure 3e). For example, as shown in Figure 3f, the NIR emission from the Ag_2S nanothermometers partially overlaps with tissue autofluorescence under 800 nm excitation. The overall spectrum changes when changing ϕ value (the relative weight of autofluorescence to Ag_2S emission), which depends on the location of the nanothermometers. If the temperature readout is obtained by analysing the FIR of I_2/I_1 or by the peak position, the calculation results from both parameters will contain the contributions from autofluorescence. The contribution of autofluorescence cannot be included in the calibration, as it will be different in each individual case, thus leading to readout errors up to several K.

Similarly, bias may also be caused by fluorescence distortion due to the absorption and scattering effects from the tissue composition (Figure 3g), in which light is attenuated in a wavelength-dependent manner. As shown in Figure 3h, the emission band shape of Ag_2S nanothermometers obtained at *in vivo* liver differs by a large amount to that obtained in subcutaneous tissue. If these distortions are erroneously attributed to temperature, it may lead to temperature readout bias of up to 40 ℃. Moreover, temperature affects the optical properties of tissues, as at a temperatures higher than 45 ℃, often used in PTT of tumours, the heat will largely affect their wavelength-dependent scattering coefficient, and subsequently alter the emission ratios and introduce error in the measured temperature.

To alleviate these unwanted biases, we suggest to carefully consider the differences in conditions and factors between the experiments that establish calibration curves and temperature sensing in the real testing scenarios. Nanothermometers with NIR excitation/emission within the optical transparency windows and lifetime-based sensing modality are highly recommended especially for *in vivo* models. In these cases, special care has to be taken to choose nanothermometers operating in spectral regions where the optical properties of tissues are wavelength-independent or, at least, known.

4. Challenges and Emerging Opportunities

In this section, we anticipate the future directions for the emerging field of nanothermometry will involve material sciences and spectral physics studies to develop the toolbox of nanothermometers with high sensitivity, accuracy and to integrate new functionalities, interface bio/nano chemistry to enable these nanothermometers to target the specific subcellular compartments, and adoptions of new imaging technologies to super resolve their distributions and dynamics. We further survey the list of ideal temperature resolution needed for monitoring the metabolism of internal organs, and suggest several recent advances and potentials to overcome the aforementioned challenges.

4.1 High brightness and relative sensitivity

Both high relative sensitivity S_R and high brightness of nanothermometers are required for their practical applications. S_R is a parameter resistant to the system variations and often being used to compare the performance of diverse material systems. The high brightness of the nanothermometer will lead to a high imaging contrast (signal-to-noise ratio), while a high S_R will result in a high temperature sensing resolution (see equation 3 in Box 1). S_R at a level of ~3%/℃ has been commonly used for imaging-based thermometry that detects temperature variations of several K (Tables 1 and 2). To improve the resolution to the sub-K range, a higher S_R is needed.
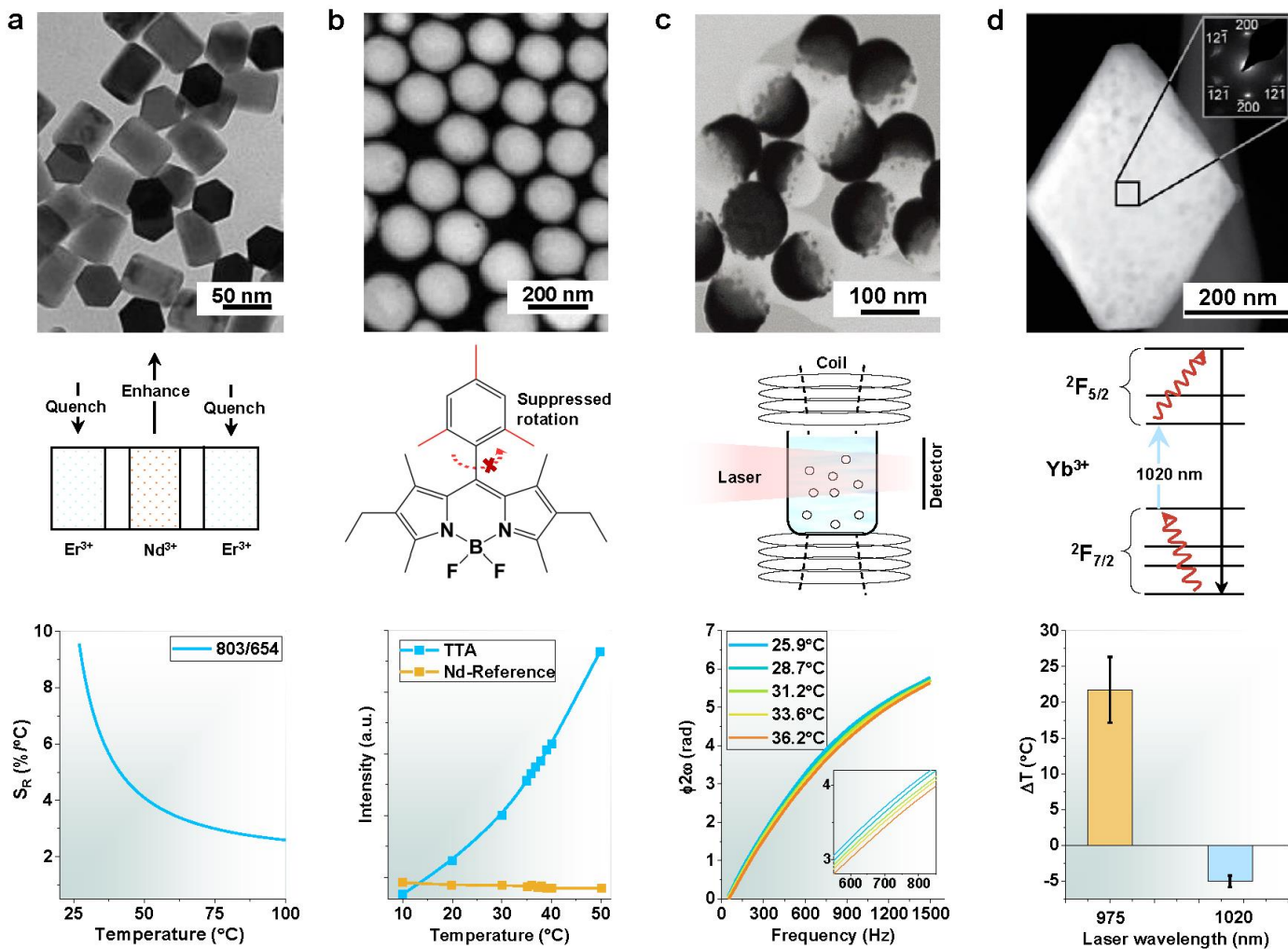
Figure 4 | New designs of temperature-responsive materials. a, Rod type heterogeneous doping with Yb^{3+}-Nd^{3+} in the core and Yb^{3+}-Er^{3+} at the tip end for thermal enhancing and quenching, in which the ratiometric emission peaks gain a high contrast and relative sensitivity with temperature increase. **b,** A TTA-UC hybrid nanothermometers showing 'turn on' integrated emission intensities (TTA, blue line) and stable reference signals (yellow line) as functions of temperature. The enhanced brightness from the TTA unit is due to the suppressed thermal deactivations of fluorescence. **c,** Simultaneous local heating and thermometry based on plasmonic magnetochromic nanoheaters. **d,** Simultaneous local cooling and thermometry based on lanthanide-doped particles.

Nearly all imaging and sensing applications will desirably require the contrast agents to be more efficient and sufficiently bright, so as to keep challenging the new limits of detection. The field of fluorescence nanothermometry is not an exception. However, there is an intrinsic issue for nearly all the fluorescent materials to date, that is, high temperature often 'kills' the brightness of a fluorescent material, which is known as thermal quenching effect. Fortunately, several recent reports show the possibility of breaking through such limit, and materials can display a positive temperature response. We recently reported that the multiphoton upconverted emissions from a type of sub-10 nm UCNPs can be enhanced by up to 2000-fold when increasing from room temperature to 453 K[12]. We have further produced a heterogeneous sandwich nanostructure by combining the thermally enhanced and quenched upconversion units and achieved a new type of ratiometric thermometer with a maximum S_R of 9.6%/°C at room temperature (Figure 4a). Independently, Li's group reported a similar design principle and made a remarkable progress in the triplet-triplet annihilation

upconversion system[9]. Figure 4b shows the nanocomposite consisting of BDM&PtTPBP organic unit and β-NaYF$_4$: 5%Nd inorganic nanocrystal. Under 635 nm excitation, BDM&PtTPBP showed a thermally enhanced upconversion at 540 nm when increasing the temperature from 283 K to 323 K, which takes advantage of the suppressed rotation of BDM annihilators. In contrast, excited by an 808 nm laser, the β-NaYF$_4$: 5%Nd nanoparticle displayed a rather constant and temperature-independent emission at 1060 nm. The simultaneous acquisitions of the orthogonal emissions at visible and NIR through by two independent laser excitations allow ratiometric sensing with a maximum S_R of ~7.1%/°C at ~22 °C. Further shifting both excitation and dual emission bands into the NIR region is essential for deep tissue applications.

4.2 New strategies for accurate sensing

More accurate temperature measurements can be achieved by independently measuring multiple parameters. The fluorescence of a nanothermometer, the velocity of a fluid, rotation rate and trap stiffness of a particle, as well as spinning of an electron, can be all sensitive to the temperature. Two or more sensing modes can be integrated in a material and studies on their responses to the external fields, such as light, mechanical and magnetic forces, microwave and plasmon hold the key to the developments of new nanothermometers. Multi-modality sensing strategies has been recently demonstrated by performing three independent measurements on a single trapped, rotating lanthanide-doped upconversion microparticle (Figure 5a)[69]. Though it shows negligible water absorption at 788 nm, the internal temperature of the microparticle was raised by the trapping laser due to the absorption of the Nd dopants, which can be measured according to both the internal and external degrees of freedom, through upconverted fluorescence, rotation rate and Brownian dynamics of the particle. Both rotation rate and trap stiffness methods, via measuring the viscosity of the surrounding medium, have achieved the same temperature sensitivity (2.0 %/°C) that was three times better than the result measured by the fluorescence method (0.66 %/°C). Figure 5b showed that the thermal loadings measured from the fluorescence and rotation rates were in a close agreement, whereas the stiffness method exhibited lower values with the differences increasing at higher trapping power. This comparison re-emphasizes the importance of cross-correlated measurements through orthogonal strategies.

The development of ratiometric nanothermometers that emit at the same wavelength by using temperature-responsive lifetimes can minimize the complex tissue interference for the fluorescence signal collection in *in vivo* thermometry. A hybrid nanoparticle, made by the combination of UCNPs, PbS QDs and a surface layer of SiO$_2$ (Figure 5c) [70], and the time-resolved method have been used to identify the intensity ratio of the dual emissions at ~810 nm from Tm^{3+} doped in UCNPs and PbS, taking advantage of the large difference in the lifetime dynamic ranges of the lanthanides at microseconds and QDs at nanoseconds (Figure 5d). This strategy led to no obvious deviation for the intensity ratios of the nanothermometers at different tissue depths (0-3 mm) (Figure 5e) while a relative sensitivity of ~ 5.6%/°C and a temperature resolution of ~ 0.5 °C at ~ 45 °C were achieved. As shown in Figure 5f, the Ratio$_{tissue blocking (1-3 mm)}$/Ratio$_{true (0 mm)}$ was close to 1 under different temperatures for the new time-resolved thermometry, indicating its immunity to tissue interference. By contrast, the conventional ratiometric thermometry suffered from obvious depth-dependent interference.
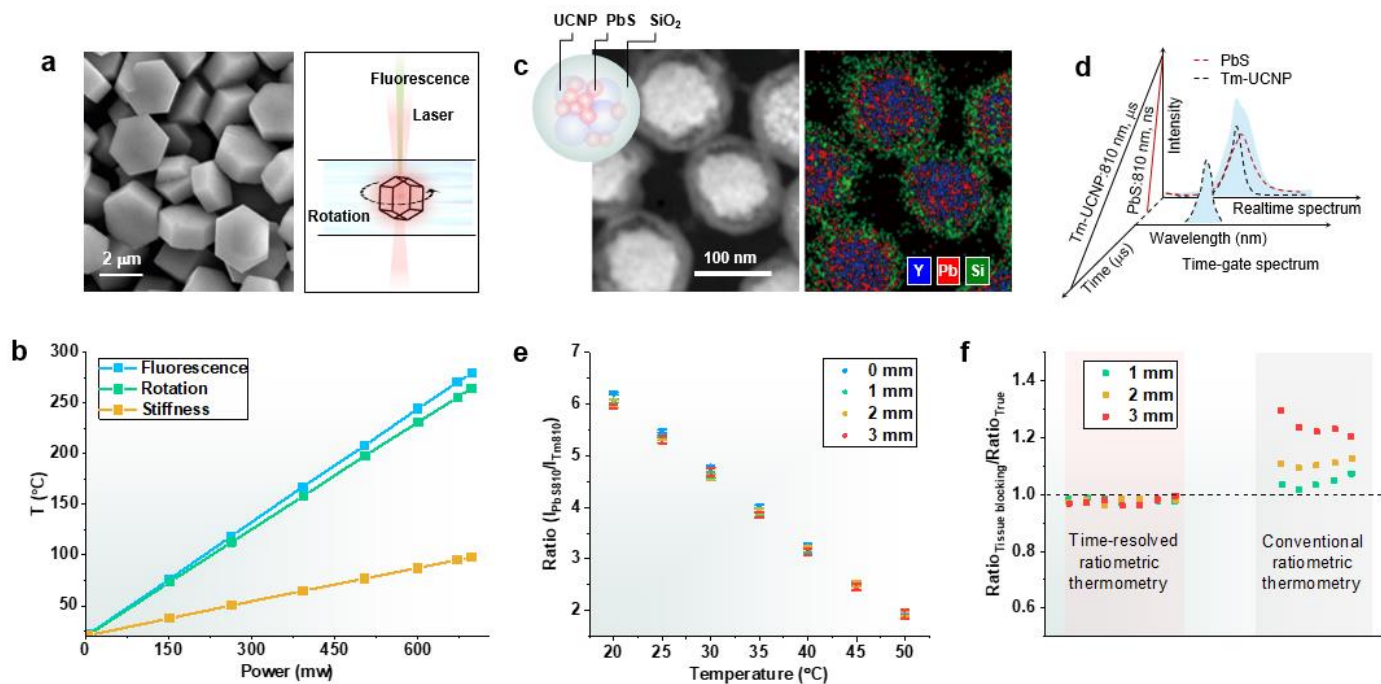
Figure 5 | Exemplified new strategies for accurate sensing. a and **b,** Tripartite method that can independently measure and correlate temperature changes from both the external and internal degrees of freedom, including fluorescence, rotation, and stiffness signals (b) for a single trapped upconversion microparticle (a). **c-f,** Time-resolved dual-emission ratiometric thermometry to minimize errors induced by tissue absorption and scattering at different depths in vivo. **c,** Structure illustration, the images of dark-field scanning TEM and corresponding EDS elemental mapping of the hybrid UCNP-PbS@SiO$_2$ nanothermometers. **d,** Schematic diagram of upconversion luminescence signals separation via time-resolved decoding. **e,** The same wavelength ratio of I$_{PbS}$ to I$_{Tm}$ obtained using time-resolved spectrometry at different temperatures and blocking with pork tissue slice of various thickness. Data and error bars, defined as s.d., were based on three measurements with an excitation of 865 nm laser on spectrometry. **f,** Ratio values deviation due to blocking with pork tissue slices of different thickness compared with ratio signals measured without pork tissue slice blocking using the time-resolved or conventional ratiometric thermometry.

Panel **a** and **b** adapted from ref. [69], © 2018 American Chemical Society. Panel **c-f** adapted from ref.[70], © The Author(s) 2020.

4.3 Active nanothermometers

Conventional nanothermometers detect local temperature changes in a passive way. There are nanomaterials can generate heating or cooling effects at the nanoscale, which are anticipated to revolutionize basic research in temperature controlled physiological conditions and applications in areas such as thermal therapies. Design and synthesis of hybrid materials to integrate nanothermometers with functional units can provide a real-time in-situ feedback system to improve the therapeutic accuracy, and reverse control of temperature (refrigeration) will play a new role in investigating the temperature effects on many physiological processes. While efficient heating sources can be relatively easy to find, including plasmonic, magnetic and carbon materials[10, 73-75] and Nd^{3+} based lanthanide materials[76, 77], cooling materials are rare. To date, only Yb^{3+} doping has been found as an effective refrigeration engine[72, 78].

Both types of active nanothermometers, e.g. hybrid nanoheater-thermometer and cooler-thermometer, can be made by core-shell nanostructures. As shown in Figure 5c, Li and coworkers developed a plasmonic magnetochromic nanoheater for simultaneous local heating and thermometry measurement[71]. The heterogeneous nanodomes were made of 100 nm diameter polystyrene beads partially coated with alternate Au/Co multiplayer. The plasmonic Au is responsible for heating, and the ferromagnetic Co responded to the applied magnetic field from coil and drove the nanodomes to rotation. As the rotating nanodomes can modulate the linearly polarized light transmission at frequency 2ω, a conventional photodiode can be used to detect the

rotation. Since the phase lag φ2ω depends solely on the local viscosity variations around the nanoparticles, the local temperature sensing can be carried out via the detection of viscosity variation of the fluid, i.e., water. The strong magnetochromic modulation allowed the detection at extremely low concentration of nanodomes, i.e., below 10^7 particles/mL, and its effectiveness was independent on the concentration. This active nanothermometer showed a temperature resolution of 0.05 °C and a maximum sensitivity of -0.028 rad/°C at room temperature. Figure 5d shows a laser cooler made from Yb^{3+} doped $LiYF_4$ nanocrystal[72, 78], in which using an appropriate laser trapping wavelength at 1020 nm, the anti-Stokes transition of Yb^{3+} can absorb heat from the local environment to lower the local temperature. By codoping Er^{3+} ions, the ratiometric fluorescence thermometry allowed the qualitative reading of cooling effect when the trapping irradiance increased. Remarkably, Roder and coworkers demonstrated that $2\%Er^{3+}$ and $10\%Yb^{3+}$codoped $LiYF_4$ can either undergo laser refrigeration ($\Delta T = -4.9 \pm 2.8$ °C) at $\lambda = 1020$ nm or heating ($\Delta T = 21.8 \pm 10.11$ °C) at $\lambda = 975$ nm[72].

4.4 Real-time super-resolution monitoring for high-spatiotemporal resolution

Live cell sensing usually comes with uncertainty from the complex environment around the nanothermometer and dynamic structure change of organelles. The pursue of more accurate temperature sensing requires high-spatiotemporal resolution, which is accessible by employing the state-of-the-art real-time super-resolution imaging techniques.

Taking an example of mitochondrion, it becomes a popular organelle in both temperature sensing and super-resolution microscopy areas, because of its' high local temperature and abundant dynamic morphological structures, presenting the phenomenological indicators of cell behaviours. ~~The real-time temperature of mitochondria is an indicator of the status of mitochondrial energetics and thus can be used to diagnose the risk of diseases ranging from diabetes and male infertility to cancer and the rate of aging. The debate around the 10^5-gap question since 2014 has not yet been concluded. According to thermodynamic equilibrium calculation, the temperature increase may only be limited to 10^{-5} K[50], however, nanothermometers detected an increase of up to several K[5, 8].~~ In 2018, Chrétien and coworkers ~~widened the gap even up to 10^6, as their data showed~~ measured that the mitochondrial temperatures were some 10 K above the surrounding water bath by using the thermometer of MitoThermo Yellow (Figure 6a)[14]. One of the major challenges to experimentally validate these results is to find out the exact locations of nanothermometers in relation to mitochondria in real time[79]. This requires the improved targeting and immobilization of nanothermometers to the specific sites within mitochondria and super resolution imaging technologies to resolve them.
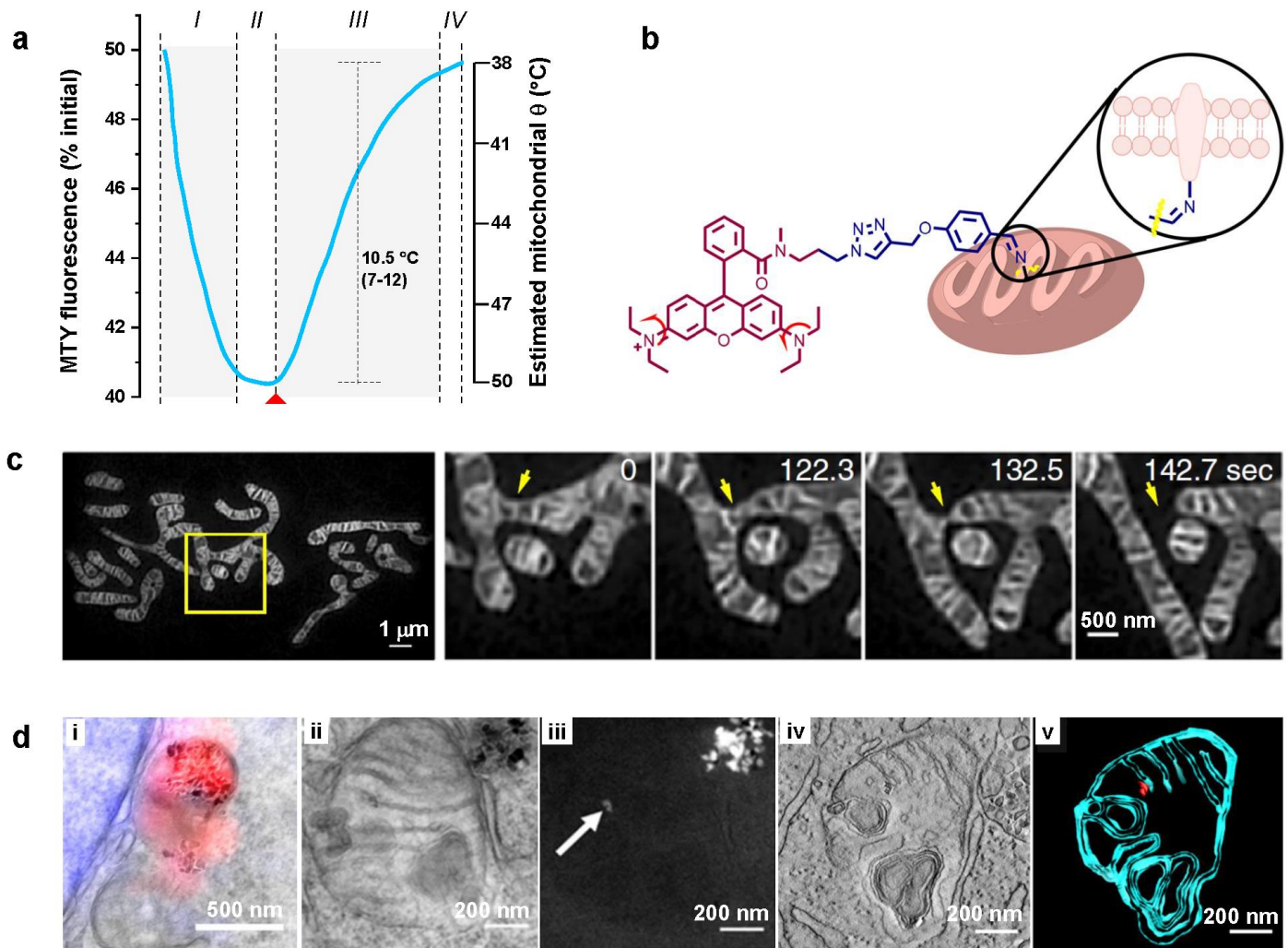
Figure 6 | Temperature monitoring and imaging of mitochondria in live cells. a, Fluorescence intensity change of MitoThermo Yellow (MTY) showing the estimated mitochondrial temperature rise of about 10 °C, by undergoing different phases (I-IV). **b,** A molecular thermometer (Mito-TEM) that designed with an anchoring unit to immobilize the probe in mitochondria. **c,** Hessian structured illumination microscopy (SIM) resolving the mitochondrial cristae structures and the fission of one mitochondrion. **d,** Correlative light-electron microscopy (CLEM) observing the individual nanodiamonds within a single cell and a mitochondrion. Panel (i) is the CLEM micrograph constructed from the overlay of LM and TEM, in which the localization of the nanodiamonds by LM is shown in red, whereas the nucleus appears in blue. Panels (ii and iii) give the brightfield TEM (ii) and dark-field energy-filtered transmission electron microscopy (EFTEM) (iii) of nanodiamonds inside a mitochondrion. Panels (iv and v) give the virtual slice from the tomogram, and the segmentation of the tomograms of single nanodiamond inside a mitochondrion.

Dye-based nanothermometers are typically used to target mitochondria[52, 82], through the electrostatic interaction formed between the membrane potential across the inner membrane of mitochondria and molecule charges. However, the electrostatic interaction is too weak to anchor the probes when the membrane potential changes at the unhealthy status of mitochondria, e.g., when exposed to CCCP. The diffusion of the nanothermometers away from mitochondria will lead to detection errors. By learning from the immobilized probes[83], *e.g.,* the MitoTracker series with the benzyl chloride group, enhanced immobilization of nanothermometers via covalent binding of chemically reactive groups could be designed and optimized. Along

this direction, Huang and co-workers developed a fixable nanothermometers Mito-TEM[51], using the benzaldehyde group to conjugate with the amino group of the protein and rhodamine B as the thermal sensing unit (Figure 6b).

To localize the nanothermometers within mitochondria, super-resolution imaging techniques are required. As the diameter of mitochondrial tubules is typically between 200 nm and 700 nm[84], and the crista-to-crista distance is often below 100 nm, the resolution of conventional optical microscopy is insufficient to see submitochondrial structures due to the diffraction limit. Diverse super-resolution microscopy techniques have been developed to resolve subcellular organelles in real-time. The latest development of structured illumination microscopy based on Hessian matrices (Hessian-SIM) allowed a large field-of-view and high-speed observation of the mitochondria inner membrane dynamics with high spatiotemporal resolutions of 88 nm and 188 Hz (Figure 6c)[80]. The recent developments of highly photostable probes have achieved super resolutions smaller than 60 nm in imaging the dynamic structure of the mitochondrial cristae in live cells using for stimulated emission depletion (STED) nanoscopy[85-87]. The correlative light-electron microscopy (CLEM) has been used to provide sub-nanometer resolution in localizing the nanoparticle-based nanothermometers (Figure 6d)[81], but EM approaches require fixing the cells.

4.5 Three dimensional real-time *in vivo* monitoring with sub 0.1 ºC resolution.

Current nanothermometry systems used for *in vivo* experiments only provide the temperature and temporal resolutions of 0.5 ºC and 2 s, respectively. This does not meet the needs of preclinical research. Temperature variations associated with *in vivo* physiological processes are around 1 ºC (Figure 7a), which requires thermal resolutions close to 0.1 ºC to accurately monitor epilepsy or acute cardiovascular accidents, such as stroke. The achieved temporal resolution of 2 s is too slow to measure single-cell hyperthermia (Figure 7b) or the fast temperature jumps that occur during epilepsy (Figure 7c). To date, nanothermometers have only been successful in providing the real-time thermal feedback during tumour hyperthermia treatments (Figure 7d). *In vivo* thermal monitoring of the fastest diseases or biological processes requires, at least, one order of magnitude reduction in time resolution down to 0.1 s.

Achieving better thermal resolution implies a requirement of reduced standard deviation σ (see equation (3) in Box 1). The obvious solution is to increase the integration time during fluorescent measurements, but it would harm the time resolution. Achievement of < 0.1 ºC, 0.1 s target calls for improved fluorescence brightness of nanothermometers to achieve high signal-to-noise fluorescence data (reduced σ) without requiring long integration times or reducing their thermal sensitivities. A promising candidate to fulfil the target of < 0.1 ºC, 0.1 s resolutions is the recently developed $Ag_2S@AgCl$ nanothermometer, fabricated through ultrafast photochemistry after the conventional wet-chemistry synthesis[88]. The ultrafast photochemistry process enhanced the quantum yield and brightness of the nanothermometer by a factor of 80.
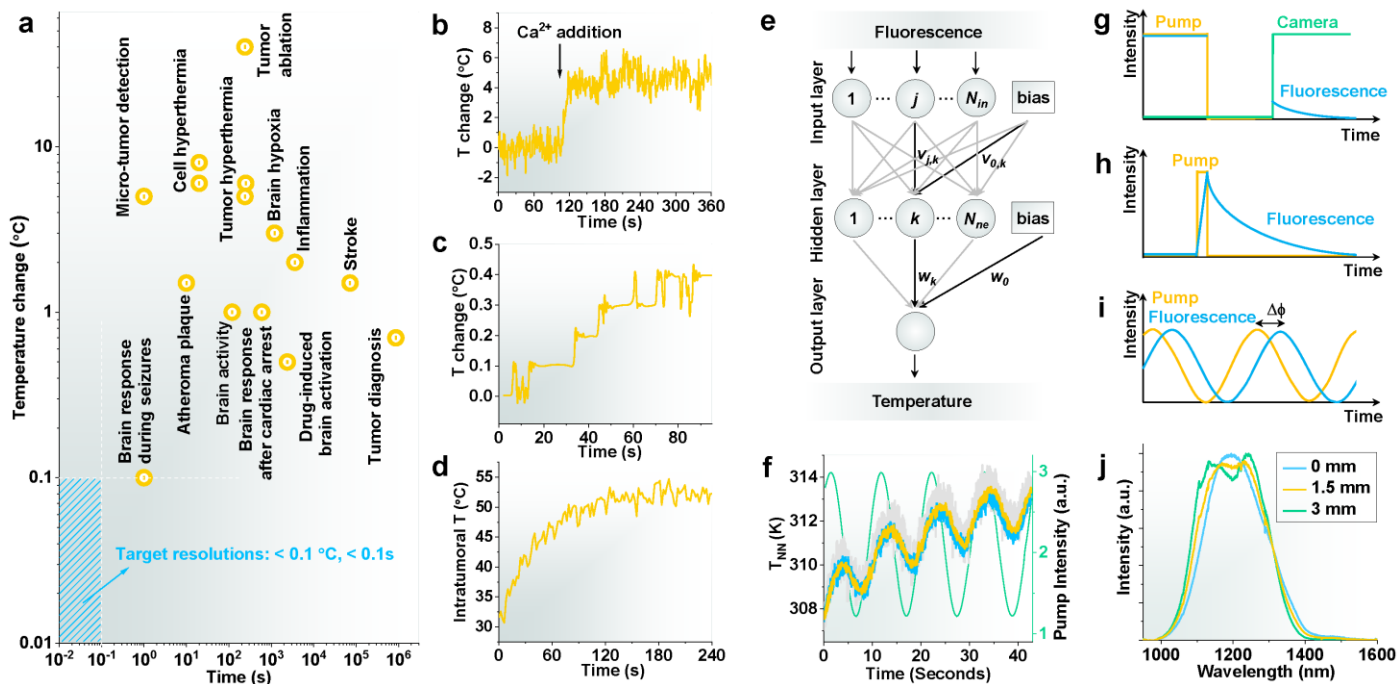
Figure 7 | High temperature resolution, reliability, and volumetric thermometry needed for *in vivo* internal organs. a, The magnitude of the temperature changes associated with different diseases or biological processes, versus the time scale at which these appear or develop. **b-d,** Time evolution of cell temperature during heat shock process (b), brain temperature during epilepsy (c), and tumour temperature during *in vivo* thermal treatment (d). **e**, Schematic showing a NN architecture with one hidden layer used in the fluorescence-based thermometry implementation. **f**, Reconstruction of photothermally induced temperature evolutions (left axis), under sinusoidal modulation (pump intensity right axis), by IP NN (gray), SP NN (blue), and multi-band NN (yellow). **g-h**, Principles of fluorescence lifetime based imaging for long lifetime nanothermometers using time gating approach (g), short lifetime nanothermometers using ps-ns laser excitation (h) and phase delay detection (i). **j,** Emission spectra of Ag_2S nanothermometers at different tissue depth.

Preclinical applications of nanothermometers do not only require the desirable resolutions but also their reliability. The complex optical properties of tissues lead to parasitic distortions in the emission spectra of nanothermometers and thereby thermal readout errors (Figure 3h). A possible solution to improving the reliability is to monitor the changes of multiple parameters, *e.g.* the whole spectral shape or multi-band emissions, and properly select the temperature calibration condition. However, the roadblock lies in the complicated inverse computation of the temperature according to the measured spectral shape with the massive features. It would be advisable to employ some emerging algorithms, *e.g.,* neural networks (NN), or even deep learning techniques to solve the inverse problem[91]. As shown in Figure 7e and 7f, Liu and co-workers reported that the spectral shape-based NN (SP-NN, input neurons N_{in}=62) or the multi-band NN (N_{in}=5) provided much higher reconstruction reliability with temperature resolutions of 0.27 K and 0.25 K, compared with the integrated intensity and peak intensity based NN (IP-NN, N_{in}=2)[90]. The benefits of the neural networks have been demonstrated in fluorescence nanothermometry, but have yet to be applied to *in vivo* measurements[90, 92, 93]. The reason for this is, very likely, the lack of experimental setups capable of fast hyperspectral *in vivo* imaging, which restricts the real-time recording of multiple spectroscopic parameters. This is changing, as

different companies launched into the market hyperspectral imagers specially designed for preclinical units that can likely be the core of reliable, fast and accurate preclinical thermal imagers.

The above-described limitations of spectral analysis-based nanothermometers could be, in principle, simultaneously solved by using lifetime-based fluorescence thermometry. Fluorescence lifetime is not affected by tissue extinction and can provide absolute temperature readouts. Measurement time (time resolution) is limited by the fluorescence lifetimes, *e.g.* tens of ns for QDs and few ms for Ln-NPs. Although numerous lifetime-based nanothermometers do exist, there is no demonstration of their potential preclinical use due to technological barriers. *In vivo* lifetime thermal imaging has been nowadays achieved by using a time gated imaging approach based on a tunable delay between excitation and acquisition (Figure 7g). This works well only for nanothermometers with lifetimes above 100 ns, not suitable for QDs nanothermometers. For short lifetimes, tens of ns, *in vivo* lifetime thermal imaging would require the use of expensive ps-ns laser pulses (Figure 7h). Alternatively, phase-modulated excitation would allow recording lifetime images by analysing the phase delay between excitation and emission intensity at each pixel (Figure 7i), in analogy with the technique used in fluorescence lifetime imaging microscopy (FLIM). The latter approach seems to be the way to overcome the challenge towards preclinical lifetime thermal imaging *in vivo*, which requires simple and low-cost excitation sources, fast cameras and the development of novel algorithms.

Any of the above-mentioned approaches for *in vivo* thermal imaging are only two-dimensional based. Three-dimensional thermal imaging requires the in-depth localization of the nanothermometers and full capture of their temperature-responsive spectroscopic parameters. On the flip side, as the magnitude of spectral distortions depends on the tissue thickness (Figure 7j), the analysis of spectra generated by nanothermometers opens a venue for direct estimation of their depth. A similar approach has been demonstrated by using the thermal emissions of objects to extract the depth dependent temperature[94]. If this is combined with lifetime thermal imaging, it is possible to build up a three-dimensional functional imaging map. For this purpose, nanothermometers with a high lifetime thermal sensitivity together with a broad emission band (so that spectral distortion is evidenced) are needed.

References

1. Brites, C.D. et al. Instantaneous ballistic velocity of suspended Brownian nanocrystals measured by upconversion nanothermometry. *Nat. Nanotechnol.* **11**, 851-856 (2016).

2. Geitenbeek, R.G. et al. In situ luminescence thermometry to locally measure temperature gradients during catalytic reactions. *ACS Catal.* **8**, 2397-2401 (2018).

3. Mi, C., Zhou, J., Wang, F., Lin, G. & Jin, D. Ultrasensitive ratiometric nanothermometer with large dynamic range and photostability. *Chem. Mater.* **31**, 9480-9487 (2019).

4. Aigouy, L., Tessier, G., Mortier, M. & Charlot, B. Scanning thermal imaging of microelectronic circuits with a fluorescent nanoprobe. *Appl. Phys. Lett.* **87**, 184105 (2005).

5. Kucsko, G. et al. Nanometre-scale thermometry in a living cell. *Nature* **500**, 54-58 (2013).

6. Kiyonaka, S. et al. Genetically encoded fluorescent thermosensors visualize subcellular thermoregulation in living cells. *Nat. Methods* **10**, 1232-1238 (2013).

7. Hattori, K. et al. ASK1 signalling regulates brown and beige adipocyte function. *Nat. Commun.* **7**, 11158 (2016).

8. Okabe, K. et al. Intracellular temperature mapping with a fluorescent polymeric thermometer and fluorescence lifetime imaging microscopy. *Nat. Commun.* **3**, 705 (2012).

9. Xu, M. et al. Ratiometric nanothermometer in vivo based on triplet sensitized upconversion. *Nat. Commun.* **9**, 2698 (2018).

10. Zhu, X. et al. Temperature-feedback upconversion nanocomposite for accurate photothermal therapy at facile temperature. *Nat. Commun.* **7**, 10437 (2016).

11. Zhu, X. et al. Upconversion nanocomposite for programming combination cancer therapy by precise control of microscopic temperature. *Nat. Commun.* **9**, 2176 (2018).

12. Zhou, J. et al. Activation of the surface dark-layer to enhance upconversion in a thermal field. *Nat. Photonics* **12**, 154-158 (2018).

13. Zhou, J., Chizhik, A.I., Chu, S. & Jin, D. Single-particle spectroscopy for functional nanomaterials. *Nature* **579**, 41-50 (2020).

14. Chrétien, D. et al. Mitochondria are physiologically maintained at close to 50 degrees C. *PLoS Biol.* **16**, e2003992 (2018).

15. Li, Q. et al. Surface-modified silicon nanoparticles with ultrabright photoluminescence and single-exponential decay for nanoscale fluorescence lifetime imaging of temperature. *J. Am. Chem. Soc.* **135**, 14924-14927 (2013).

16. Kalytchuk, S. et al. Carbon dot nanothermometry: Intracellular photoluminescence lifetime thermal sensing. *ACS Nano* **11**, 1432-1442 (2017).

17. Varshni, Y.P. Temperature dependence of the energy gap in semiconductors. *Physica* **34**, 149-154 (1967).

18. Maestro, L.M. et al. CdSe quantum dots for two-photon fluorescence thermal imaging. *Nano Lett.* **10**, 5109-5115 (2010).

19. Maestro, L.M. et al. CdTe quantum dots as nanothermometers: towards highly sensitive thermal imaging. *Small* **7**, 1774-1778 (2011).

20. Vetrone, F. et al. Temperature sensing using fluorescent nanothermometers. *ACS nano* **4**, 3254-3258 (2010).

21. Balabhadra, S. et al. Boosting the sensitivity of Nd^{3+}-based luminescent nanothermometers. *Nanoscale* **7**, 17261-17267 (2015).

22. Senapati, S. & Nanda, K.K. Red emitting Eu:ZnO nanorods for highly sensitive fluorescence intensity ratio based optical thermometry. *J. Mater. Chem. C* **5**, 1074-1082 (2017).

23. Donner, J.S., Thompson, S.A., Kreuzer, M.P., Baffou, G. & Quidant, R. Mapping intracellular temperature using green fluorescent protein. *Nano Lett.* **12**, 2107-2111 (2012).

24. Zondervan, R., Kulzer, F., van der Meer, H., Disselhorst, J.A. & Orrit, M. Laser-driven microsecond temperature cycles analyzed by fluorescence polarization microscopy. *Biophys. J.* **90**, 2958-2969 (2006).

25. Neumann, P. et al. High-precision nanoscale temperature sensing using single defects in diamond. *Nano Lett.* **13**, 2738-2742 (2013).

26. Tsai, P.C. et al. Measuring nanoscale thermostability of cell membranes with single gold-diamond nanohybrids. *Angew. Chem. Int. Ed. Engl.* **56**, 3025-3030 (2017).

27. Huang, H., Delikanli, S., Zeng, H., Ferkey, D.M. & Pralle, A. Remote control of ion channels and neurons through magnetic-field heating of nanoparticles. *Nat. Nanotechnol.* **5**, 602-606 (2010).

28. Tsuji, T., Ikado, K., Koizumi, H., Uchiyama, S. & Kajimoto, K. Difference in intracellular temperature rise between matured and precursor brown adipocytes in response to uncoupler and β-adrenergic agonist stimuli. *Sci. Rep.* **7**, 12889 (2017).

29. Kimura, H. et al. The thermogenic actions of natriuretic peptide in brown adipocytes: The direct measurement of the intracellular temperature using a fluorescent thermoprobe. *Sci. Rep.* **7**, 12978 (2017).

30. Kato, H. et al. ER-resident sensor PERK is essential for mitochondrial thermogenesis in brown adipose tissue. *Life Sci. Alliance* **3**, e201900576 (2020).

31. Hoshi, Y. et al. Ischemic brain injury leads to brain edema via hyperthermia-induced TRPV4 activation. *J. Neurosci.* **38**, 5700-5709 (2018).

32. Rexius-Hall, M.L., Uchiyama, S., Eddington, D. & Rehman, J. Glycolysis is required for rapid adipocyte thermogenesis induced by cold stress. *FASEB J.* **31**, suppl. 886.814 (2017).

33. Choi, J. et al. Probing and manipulating embryogenesis via nanoscale thermometry and temperature control. *arXiv preprint arXiv:2001.02664* (2020).

34. Nakano, M. et al. Genetically encoded ratiometric fluorescent thermometer with wide range and rapid response. *PloS one* **12**, e0172344 (2017).

35. Savchuk, O.A., Silvestre, O.F., Adão, R.M.R. & Nieder, J.B. GFP fluorescence peak fraction analysis based nanothermometer for the assessment of exothermal mitochondria activity in live cells. *Sci. Rep.* **9**, 7535 (2019).

36. Kriszt, R. et al. Optical visualisation of thermogenesis in stimulated single-cell brown adipocytes. *Sci. Rep.* **7**, 1383 (2017).

37. Xie, T.R., Liu, C.F. & Kang, J.S. Dye-based mito-thermometry and its application in thermogenesis of brown adipocytes. *Biophys. Rep.* **3**, 85-91 (2017).

38. Jenkins, J., Borisov, S.M., Papkovsky, D.B. & Dmitriev, R.I. Sulforhodamine nanothermometer for multiparametric fluorescence lifetime imaging microscopy. *Anal. Chem.* **88**, 10566-10572 (2016).

39. Arai, S., Lee, S.C., Zhai, D., Suzuki, M. & Chang, Y.T. A molecular fluorescent probe for targeted visualization of temperature

at the endoplasmic reticulum. *Sci. Rep.* **4**, 6701 (2014).

40. Yang, J.M., Yang, H. & Lin, L. Quantum dot nano thermometers reveal heterogeneous local thermogenesis in living cells. *ACS Nano* **5**, 5067-5071 (2011).

41. Donner, J.S. et al. Imaging of plasmonic heating in a living organism. *ACS Nano* **7**, 8666-8672 (2013).

42. Arai, S. et al. Micro-thermography in millimeter-scale animals by using orally-dosed fluorescent nanoparticle thermosensors. *Analyst* **140**, 7534-7539 (2015).

43. Gota, C., Okabe, K., Funatsu, T., Harada, Y. & Uchiyama, S. Hydrophilic fluorescent nanogel thermometer for intracellular thermometry. *J. Am. Chem. Soc.* **131**, 2766-2767 (2009).

44. Tsuji, T., Yoshida, S., Yoshida, A. & Uchiyama, S. Cationic fluorescent polymeric thermometers with the ability to enter yeast and mammalian cells for practical intracellular temperature measurements. *Anal. Chem.* **85**, 9815-9823 (2013).

45. Oyama, K. et al. Walking nanothermometers: spatiotemporal temperature measurement of transported acidic organelles in single living cells. *Lab Chip* **12**, 1591-1593 (2012).

46. Takei, Y. et al. A nanoparticle-based ratiometric and self-calibrated fluorescent thermometer for single living cells. *ACS Nano* **8**, 198-206 (2014).

47. Tanimoto, R. et al. Detection of temperature difference in neuronal cells. *Sci. Rep.* **6**, 22071 (2016).

48. Jin, D. et al. Nanoparticles for super-resolution microscopy and single-molecule tracking. *Nat. Methods* **15**, 415-423 (2018).

49. Simpson, D.A. et al. Non-neurotoxic nanodiamond probes for intraneuronal temperature mapping. *ACS Nano* **11**, 12077-12086 (2017).

50. Baffou, G., Rigneault, H., Marguet, D. & Jullien, L. A critique of methods for temperature imaging in single cells. *Nat. Methods* **11**, 899-901 (2014).

51. Huang, Z., Li, N., Zhang, X., Wang, C. & Xiao, Y. Fixable molecular thermometer for real-time visualization and quantification of mitochondrial temperature. *Anal. Chem.* **90**, 13953-13959 (2018).

52. Arai, S. et al. Mitochondria-targeted fluorescent thermometer monitors intracellular temperature gradient. *Chem. Commun.* **51**, 8044-8047 (2015).

53. Hayashi, T., Fukuda, N., Uchiyama, S. & Inada, N. A cell-permeable fluorescent polymeric thermometer for intracellular temperature mapping in mammalian cell lines. *PloS one* **10**, e0117677 (2015).

54. Qiao, J. et al. Ratiometric fluorescent polymeric thermometer for thermogenesis investigation in living cells. *Anal. Chem.* **87**, 10535-10541 (2015).

55. Qiao, J. et al. Simultaneous monitoring of mitochondrial temperature and ATP fluctuation using fluorescent probes in living cells. *Anal. Chem.* **90**, 12553-12558 (2018).

56. Carrasco, E. et al. Intratumoral thermal reading during photo-thermal therapy by multifunctional fluorescent nanoparticles. *Adv. Funct. Mater.* **25**, 615-626 (2015).

57. Ximendes, E.C. et al. Unveiling in vivo subcutaneous thermal dynamics by infrared luminescent nanothermometers. *Nano Lett.* **16**, 1695-1703 (2016).

58. Ximendes, E.C. et al. In vivo subcutaneous thermal video recording by supersensitive infrared nanothermometers. *Adv. Funct. Mater.* **27**, 1702249 (2017).

59. del Rosal, B. et al. Infrared-emitting QDs for thermal therapy with real-time subcutaneous temperature feedback. *Adv. Funct. Mater.* **26**, 6060-6068 (2016).

60. Ximendes, E.C. et al. In vivo ischemia detection by luminescent nanothermometers. *Adv. Healthc. Mater.* **6**, 1601195 (2017).

61. Santos, H.D.A. et al. In vivo early tumor detection and diagnosis by infrared luminescence transient nanothermometry. *Adv. Funct. Mater.* **28**, 1803924 (2018).

62. del Rosal, B. et al. In vivo contactless brain nanothermometry. *Adv. Funct. Mater.* **28**, 1806088 (2018).

63. Deepankumar, K. et al. Temperature sensing using red fluorescent protein. *Biotechnol. Bioproc. E.* **20**, 67-72 (2015).

64. Ferdinandus, A.S., Takeoka, S., Ishiwata, S.i., Suzuki, M. & Sato, H. Facilely fabricated luminescent nanoparticle thermosensor for real-time microthermography in living animals. *ACS Sensors* **1**, 1222-1227 (2016).

65. Jaque, D. et al. Nanoparticles for photothermal therapies. *Nanoscale* **6**, 9494-9530 (2014).

66. Senden, T., Rabouw, F.T. & Meijerink, A. Photonic effects on the radiative decay rate and luminescence quantum yield of doped nanocrystals. *ACS Nano* **9**, 1801-1808 (2015).

67. Shen, Y., Lifante, J., Fernández, N., Jaque, D. & Ximendes, E. In vivo spectral distortions of infrared luminescent

nanothermometers compromise their reliability. *ACS Nano* **Accepted** (2020).

68. Liu, P.Y. et al. Cell refractive index for cell biology and disease diagnosis: past, present and future. *Lab Chip* **16**, 634-644 (2016).

69. Rodríguez-Sevilla, P., Arita, Y., Liu, X., Jaque, D. & Dholakia, K. The temperature of an optically trapped, rotating microparticle. *ACS Photonics* **5**, 3772-3778 (2018).

70. Qiu, X. et al. Ratiometric upconversion nanothermometry with dual emission at the same wavelength decoded via a time-resolved technique. *Nat. Commun.* **11**, 4 (2020).

71. Li, Z. et al. Simultaneous local heating/thermometry based on plasmonic magnetochromic nanoheaters. *Small* **14**, e1800868 (2018).

72. Roder, P.B., Smith, B.E., Zhou, X., Crane, M.J. & Pauzauskie, P.J. Laser refrigeration of hydrothermal nanocrystals in physiological media. *Proc. Natl. Acad. Sci. USA* **112**, 15024-15029 (2015).

73. Rodríguez-Sevilla, P. et al. Thermal Scanning at the Cellular Level by an Optically Trapped Upconverting Fluorescent Particle. *Adv. Mater.* **28**, 2421-2426 (2016).

74. Chan, M.S. et al. Stepwise ligand-induced self-assembly for facile fabrication of nanodiamond-gold nanoparticle dimers via noncovalent biotin-streptavidin interactions. *Nano Lett.* **19**, 2020-2026 (2019).

75. Piñol, R. et al. Joining time-resolved thermometry and magnetic-induced heating in a single nanoparticle unveils intriguing thermal properties. *ACS Nano* **9**, 3134-3142 (2015).

76. Suo, H., Zhao, X., Zhang, Z. & Guo, C. 808 nm light-triggered thermometer-heater upconverting platform based on Nd^{3+}-sensitized yolk-shell $GdOF@SiO_2$. *ACS Appl. Mater. Interfaces* **9**, 43438-43448 (2017).

77. Marciniak, L., Pilch, A., Arabasz, S., Jin, D. & Bednarkiewicz, A. Heterogeneously Nd^{3+} doped single nanoparticles for NIR-induced heat conversion, luminescence, and thermometry. *Nanoscale* **9**, 8288-8297 (2017).

78. Rahman, A.T.M.A. & Barker, P.F. Laser refrigeration, alignment and rotation of levitated Yb^{3+}:YLF nanocrystals. *Nat. Photonics* **11**, 634-638 (2017).

79. Lane, N. Hot mitochondria? *PLoS Biol.* **16**, e2005113 (2018).

80. Huang, X. et al. Fast, long-term, super-resolution imaging with Hessian structured illumination microscopy. *Nat. Biotechnol.* **36**, 451-459 (2018).

81. Han, S. et al. High-contrast imaging of nanodiamonds in cells by energy filtered and correlative light-electron microscopy: toward a quantitative nanoparticle-cell analysis. *Nano Lett.* **19**, 2178-2185 (2019).

82. Homma, M., Takei, Y., Murata, A., Inoue, T. & Takeoka, S. A ratiometric fluorescent molecular probe for visualization of mitochondrial temperature in living cells. *Chem. Commun.* **51**, 6194-6197 (2015).

83. Zhang, X., Sun, Q., Huang, Z., Huang, L. & Xiao, Y. Immobilizable fluorescent probes for monitoring the mitochondria microenvironment: a next step from the classic. *J. Mater. Chem. B* **7**, 2749-2758 (2019).

84. Jakobs, S., Stephan, T., Ilgen, P. & Brüser, C. Light microscopy of mitochondria at the nanoscale. *Annu. Rev. Biophys.* **49**, 291-310 (2020).

85. Stephan, T., Roesch, A., Riedel, D. & Jakobs, S. Live-cell STED nanoscopy of mitochondrial cristae. *Sci. Rep.* **9**, 12419 (2019).

86. Yang, X. et al. Mitochondrial dynamics quantitatively revealed by STED nanoscopy with an enhanced squaraine variant probe. *bioRxiv*, 646117 (2019).

87. Wang, C. et al. A photostable fluorescent marker for the superresolution live imaging of the dynamic structure of the mitochondrial cristae. *Proc. Natl. Acad. Sci. USA* **116**, 15817-15822 (2019).

88. Santos, H.D.A. et al. Ultrafast photochemistry produces superbright NIR-II dots for low-dose in vivo imaging. *Nat. Commun.* **Accepted** (2020).

89. Yang, X.F., Chang, J.H. & Rothman, S.M. Intracerebral temperature alterations associated with focal seizures. *Epilepsy Res.* **52**, 97-105 (2002).

90. Liu, L. et al. Wideband fluorescence-based thermometry by neural network recognition: Photothermal application with 10 ns time resolution. *J. Appl. Phys.* **118**, 184906 (2015).

91. Zhou, J., Huang, B., Yan, Z. & Bünzli, J.-C.G. Emerging role of machine learning in light-matter interaction. *Light Sci. Appl.* **8**, 84 (2019).

92. Munro, T., Liu, L., Glorieux, C. & Ban, H. CdSe/ZnS quantum dot fluorescence spectra shape-based thermometry via neural network reconstruction. *J. Appl. Phys.* **119**, 214903 (2016).

93. Liu, L. et al. Fluorescence spectra shape based dynamic thermometry. *Appl. Phys. Lett.* **104**, 031902 (2014).

94. Xiao, Y., Wan, C., Shahsafi, A., Salman, J. & Kats, M.A. Depth thermography: noninvasive 3D temperature profiling using infrared thermal emission. *ACS Photonics* **7**, 853-860 (2020).

Acknowledgement